

## COAMPS<sup>®</sup>-LES: MODEL EVALUATION AND ANALYSIS OF SECOND-AND THIRD-MOMENT VERTICAL VELOCITY BUDGETS

JEAN-CHRISTOPHE GOLAZ\*, SHOUPING WANG<sup>1</sup>, JAMES D. DOYLE<sup>1</sup>  
and JEROME M. SCHMIDT<sup>1</sup>

*National Research Council, Naval Research Laboratory, Monterey, CA, U.S.A.*

<sup>1</sup>*Naval Research Laboratory, Monterey, CA, U.S.A*

(Received in final form 5 November 2004)

**Abstract.** The Naval Research Laboratory Coupled Ocean/Atmosphere Mesoscale Prediction System (COAMPS<sup>®</sup>) has been extended to perform as a large-eddy simulation (LES) model. It has been validated with a series of boundary-layer experiments spanning a range of cloud nighttime, and includes a nighttime stratocumulus case, a trade wind cumulus layer, shallow cumulus convection over land, and a mixed regime consisting of cumulus clouds under broken stratocumulus. COAMPS-LES results are in good agreement with other models for all the cases simulated. Exact numerical budgets for the vertical velocity second ( $\overline{w'^2}$ ) and third moment ( $\overline{w'^3}$ ) have been derived for the stratocumulus and trade wind cumulus cases. For the  $\overline{w'^3}$  budget in the stratocumulus, the buoyancy contribution from the updraughts and downdraughts largely cancel each other due to their similar magnitudes but opposite signs. In contrast, for the cumulus layer, the negative buoyancy contribution from the environmental downdraughts is negligible and the positive contribution from the updraughts completely dominates due to the conditional instability in the environment. As a result,  $\overline{w'^3}$  is significantly larger in the cumulus than in the stratocumulus layer.

**Keywords:** Cumulus, Large-eddy simulation, Moments, Stratocumulus, Turbulence budgets.

### 1. Introduction

Large-eddy simulation (LES) models have become increasingly useful as tools for the study of the atmospheric boundary-layer with increases in computer power. By definition, LES models have a sufficiently small grid increment to explicitly resolve the large energy-carrying eddies in the boundary-layer, while parameterizing the smaller ones. A review of the LES modelling technique can be found in Mason (1994); LES of boundary-layer clouds is not new. For example, Sommeria (1976) and Nicholls et al. (1982) simulated shallow cumulus clouds and Deardorff (1980) simulated a stratocumulus-topped boundary-layer several decades ago. However, advances in computational power have rendered LES much more affordable and ubiquitous. At the same time, these advances have also allowed traditional mesoscale models to be used for numerical weather forecasts at

\* E-mail: golaz@nrlmry.navy.mil

progressively smaller grid increments. In the not so distant future, it is probable that some specialised forecasts will be performed in real time with a horizontal grid spacing of the order of hundreds of metres, approaching what is typically considered part of the LES regime. Therefore, there is a natural interest in using existing mesoscale models for LES applications.

One such mesoscale model is the Naval Research Laboratory's Coupled Ocean/Atmosphere Mesoscale Prediction System (COAMPS<sup>®</sup>; Hodur, 1997). We have extended its atmospheric component to perform as a LES by adding two subgrid-scale mixing schemes: the first one is a local equilibrium model and the second a turbulence kinetic energy (TKE) scheme. The extended model, referred hereafter to as COAMPS-LES, has been validated using a number of test cases representing a range of different boundary-layer cloud regimes. They were selected from intercomparison studies for which extensive published results exist. Glendening and Haack (2001) used a previous version of COAMPS as a LES model, but their work was not implemented in the latest parallel version of the code and was not tested for cloudy boundary layers.

From our simulations of boundary-layer clouds, we have derived exact numerical budgets (within machine precision) of the second ( $\overline{w'^2}$ ) and third moment ( $\overline{w'^3}$ ) of the vertical velocity  $w$ . Second-moment budgets have been studied fairly extensively (e.g. Moeng, 1986; Cuijpers et al., 1996; de Roode and Bretherton, 2003). Closely related to the  $\overline{w'^2}$  budget is the TKE budget, which has received considerable attention. For example, Grant and Lock (2004) analysed the TKE budgets of a series of LESs of shallow cumulus convection using the similarity framework proposed by Grant and Brown (1999). Budgets of  $\overline{w'^3}$  have comparatively received little attention. To our knowledge, the only full LES-derived budget published of a cloudy boundary-layer is a shallow cumulus case from Cuijpers et al. (1996). The  $\overline{w'^3}$  budget is particularly interesting because  $\overline{w'^3}$  provides information about the organization of the turbulence and can vary significantly from one cloud regime to another. Also, some boundary-layer parameterizations now include predictive equations for  $\overline{w'^2}$  and  $\overline{w'^3}$  (e.g. Lappen and Randall, 2001; Golaz et al., 2002), hence sparking fresh interest in higher moment  $w$  budgets.

The organization of the paper is as follows. Section 2 briefly describes COAMPS and the LES modifications that were made. Section 3 presents an overview of the validation test cases and compares COAMPS-LES results with other models. The vertical velocity higher moment budgets are introduced and discussed in Section 4. Finally, we summarize our findings in Section 5.

## 2. Model Description

The LES model is based on COAMPS (Hodur, 1997). We only present a brief overview of the base model and emphasize the LES related alterations. The

prognostic variables consist of the Cartesian wind components ( $u_i$ ,  $i = 1, 2, 3$ ), the perturbation Exner function ( $\pi'$ ), the dry potential temperature ( $\theta$ ), the water vapour and cloud water mixing ratios ( $q_v$ ,  $q_c$ ). The dynamics is governed by the compressible form of the Navier–Stokes equations (Klemp and Wilhelmson, 1978). The prognostic equations are:

$$\begin{aligned} \frac{\partial u_i}{\partial t} + c_p \theta_{v,0} \frac{\partial \pi'}{\partial x_i} = & -u_j \frac{\partial u_i}{\partial x_j} + g \left( \frac{\theta - \theta_0}{\theta_0} + \frac{1 - \epsilon_0}{\epsilon_0} q_v - q_c \right) \delta_{i3} \\ & + \epsilon_{ij3} f u_j + \frac{\partial \tau_{ij}}{\partial x_j} + \nu \nabla_H^4 u_i, \end{aligned} \quad (1)$$

$$\frac{\partial \pi'}{\partial t} + \frac{c_0^2}{c_p \rho_0 \theta_{v,0}^2} \frac{\partial}{\partial x_j} (\rho_0 \theta_{v,0} u_j) = -u_j \frac{\partial \pi'}{\partial x_j} - \frac{R_d \pi_0}{c_v} \frac{\partial u_j}{\partial x_j} + \frac{c_0^2}{c_p \theta_{v,0}^2} \frac{d\theta_v}{dt}, \quad (2)$$

$$\frac{\partial \theta}{\partial t} = -u_j \frac{\partial \theta}{\partial x_j} - \frac{\partial H_{\theta,j}}{\partial x_j} + S_{\theta,\text{rad}} + S_{\theta,\text{CE}}, \quad (3)$$

$$\frac{\partial q_v}{\partial t} = -u_j \frac{\partial q_v}{\partial x_j} - \frac{\partial H_{q_v,j}}{\partial x_j} + S_{q_v,\text{CE}}, \quad (4)$$

$$\frac{\partial q_c}{\partial t} = -u_j \frac{\partial q_c}{\partial x_j} - \frac{\partial H_{q_c,j}}{\partial x_j} + S_{q_c,\text{CE}}. \quad (5)$$

Here,  $R_d$  is the dry air gas constant,  $R_v$  is the water vapour gas constant and  $\epsilon_0 = R_d/R_v$ ;  $c_p$  is the specific heat at constant pressure and  $c_v$  the specific heat at constant volume;  $g$  is the acceleration due to gravity and  $f$  the Coriolis parameter. A height varying reference state is defined by  $\rho_0$ ,  $\theta_0$ ,  $\theta_{v,0}$ ,  $\pi_0$  such that the state is in hydrostatic balance.  $c_0$  is the speed of sound of the reference state;  $\frac{d\theta_v}{dt}$  is the total diabatic heating;  $\tau_{ij}$  is the turbulent subgrid-scale momentum flux and  $H_{\psi,j}$  the turbulent scalar flux where  $\psi = \{\theta, q_v, q_c\}$ ;  $S_{\theta,\text{rad}}$  represents the time rate of change of  $\theta$  due to radiative heating or cooling,  $S_{\psi,\text{CE}}$  the time rate of change of  $\psi$  due to condensation and evaporation.

Equations (1)–(5) are discretized on an Arakawa C grid. Although a number of projections options are available in COAMPS, only the Cartesian projection is used for this work. The time stepping for the dynamical variables (1)–(2) is leapfrog, and for the thermodynamic variables (3)–(5), a choice of leapfrog or forward-in-time is available. A small acoustic time step is used to stably integrate the terms on the left-hand side of (1)–(2). Fourth-order horizontal numerical diffusion with coefficient  $\nu$  and a Robert filter are applied to all leapfrog variables. Advection options include second- and fourth-order centred schemes, as well as the positive definite Bott scheme (Bott, 1989a, b) with second- and fourth-order polynomial interpolation for the thermodynamic variables. Because the Bott advection scheme is written in a conservative flux form, the advection terms in (3)–(5) are rewritten as:

$$-u_j \frac{\partial \psi}{\partial x_j} = -\frac{1}{\rho_0} \frac{\partial}{\partial x_j} (\rho_0 u_j \psi) + \frac{\psi}{\rho_0} \frac{\partial}{\partial x_j} (\rho_0 u_j), \quad (6)$$

where the divergence term on the right-hand side (RHS) is computed in a manner consistent with the Bott advection. In all simulations presented here, we integrate the dynamical equations (1)–(2) using leapfrog time stepping in conjunction with second-order centred advection, and the thermodynamic equations (3)–(5) using forward-in-time and Bott's advection option using second-order polynomial interpolation.

Following Lilly (1962), the subgrid-scale turbulent fluxes are written as:

$$\tau_{ij} = K_M D_{ij} = K_M \left( \frac{\partial u_i}{\partial x_j} + \frac{\partial u_j}{\partial x_i} - \frac{2}{3} \frac{\partial u_j}{\partial x_j} \right), \quad (7)$$

$$H_{\psi,j} = -K_H \frac{\partial \psi}{\partial x_j}. \quad (8)$$

$D_{ij}$  is the deformation tensor,  $K_M$  and  $K_H$  are the eddy viscosity and eddy diffusion coefficients, which are computed using either one of the two subgrid-scale schemes described below. The first one is a prognostic subgrid-scale TKE scheme and the second one is a local equilibrium model.

## 2.1. SUBGRID-SCALE TKE MODEL

The history of subgrid-scale TKE models for large eddy simulations of the cloudy atmospheric boundary-layer dates back to the work of Deardorff (1980). The prognostic equation for the TKE,  $e$ , is given by:

$$\frac{\partial e}{\partial t} = -u_j \frac{\partial e}{\partial x_j} + \tau_{ij} \frac{\partial u_i}{\partial x_j} + \frac{g}{\theta_0} \overline{w''\theta_v''} - \frac{\partial}{\partial x_j} \left( \overline{u_j'' e} + \frac{\overline{u_j'' p''}}{\rho_0} \right) - \epsilon. \quad (9)$$

The terms on the RHS respectively represent advection, shear production, buoyancy production, turbulence transport, and dissipation. The eddy viscosity and diffusion coefficients are:

$$K_M = c_m \tilde{f} l e^{1/2}, \quad (10)$$

$$K_H = \left( c_{h1} + c_{h2} \frac{l}{\Delta} \right) \tilde{f} l e^{1/2}, \quad (11)$$

where  $\Delta$  is the grid length scale and  $l$  the mixing length scale;  $\tilde{f}$  is a factor to be derived later to account for the reduction in the mixing length near the surface.

To be valid for both clear and cloudy air, the buoyancy production term in (9) is expressed in terms of conserved variables:

$$\overline{w''\theta_v''} = A\overline{w''\theta_l''} + B\overline{w''q_t''} = -K_H \left( A \frac{\partial \theta_l}{\partial z} + B \frac{\partial q_t}{\partial z} \right), \quad (12)$$

where  $\theta_l$  is the liquid water potential temperature and  $q_t = q_v + q_c$  the total water mixing ratio. The functions  $A$  and  $B$  are taken from Cuijpers and Duynkerke (1993) and have different expressions for unsaturated and saturated air. The saturated values are used for interior cloud points and the unsaturated values for cloud edges and clear air.

The turbulence transport term is modelled as

$$\overline{u_j''e} + \frac{\overline{u_j''p''}}{\rho_0} = -2K_M \frac{\partial e}{\partial x_j}, \quad (13)$$

and the dissipation as

$$\epsilon = \left( c_{\epsilon 1} + c_{\epsilon 2} \frac{l}{\Delta} \right) \frac{e^{3/2}}{f\tilde{l}}. \quad (14)$$

The grid length scale,  $\Delta$ , is a function only of the grid spacing

$$\Delta = (\Delta x \Delta y \Delta z)^{1/3} \quad (15)$$

whereas the mixing length scale  $l$  is allowed to become smaller than the grid length scale in stably stratified flows:

$$l = \min \left( \sqrt{\frac{2}{3} \frac{e}{N^2}}, \Delta \right). \quad (16)$$

$N^2$  is the moist Brunt–Väisälä frequency consistent with the buoyancy term (12):

$$N^2 = \frac{g}{\theta_0} \left( A \frac{\partial \theta_l}{\partial z} + B \frac{\partial q_t}{\partial z} \right). \quad (17)$$

The values of the numerical coefficients follow Stevens et al. (1999):  $c_m = 0.0856$ ,  $c_{h1} = c_m$ ,  $c_{h2} = 0.1184$ ,  $c_{\epsilon 1} = 0.1911$ ,  $c_{\epsilon 2} = 0.6539$ .

## 2.2. SUBGRID-SCALE LOCAL EQUILIBRIUM MODEL

This category of subgrid-scale model is frequently referred to as Lilly–Smagorinsky after Lilly (1962) and Smagorinsky (1963). As shown by Stevens et al. (1999), it can be directly derived from Equations (9)–(11) assuming that the TKE is in local equilibrium (i.e. neglecting storage, advection, turbulence transport in Equation (9) and solving for  $e$ ). Furthermore, assuming that  $l = \Delta$ , one obtains:

$$K_M = \lambda^2 \left[ \max \left( S^2 - \frac{c_{h1} + c_{h2}}{c_m} N^2, 0 \right) \right]^{1/2}, \quad (18)$$

$$K_H = \frac{c_{h1} + c_{h2}}{c_m} K_M, \quad (19)$$

with  $\lambda$  defined as

$$\lambda = c_s \tilde{f} \Delta. \quad (20)$$

$c_s$  is given by  $c_s = (c_m^3 / (c_{\epsilon 1} + c_{\epsilon 2}))^{1/4}$ . The max function in Equation (18) has only been introduced to ensure that  $K_M$  remains positive definite. The deformation,  $S^2$ , is

$$S^2 = \frac{1}{2} (D_{ij})^2 = D_{ij} \frac{\partial u_i}{\partial x_j}. \quad (21)$$

The mixing length correction factor  $\tilde{f}$  is derived by requiring that  $\lambda$  reduces to  $\kappa(z + z_0)$  near the surface. This is accomplished using the same matching function as Brown et al. (1994):

$$\frac{1}{\lambda^2} = \frac{1}{(c_s \Delta)^2} + \frac{1}{(\kappa(z + z_0))^2}, \quad (23)$$

where  $\kappa$  is the von Karman constant and  $z_0$  the roughness length. Substituting (20) into (22) and solving for  $\tilde{f}$  gives:

$$\tilde{f} = \left\{ 1 + \left( \frac{c_s \Delta}{\kappa(z + z_0)} \right)^2 \right\}^{-1/2}. \quad (23)$$

This last expression is used for the two subgrid-scale models, therefore ensuring that they share equivalent near-surface mixing lengths.

### 3. Model Validation

The COAMPS-LES code was validated by performing a series of reference simulations. They were all selected from the growing database of Global Energy and Water Cycle Experiment Cloud System Study (GCSS) inter-comparison studies. We chose four cases that span a range of different boundary-layer cloud regimes. The first case is a nocturnal stratocumulus case loosely based on 7 July 1987 from the First International Satellite Cloud Climatology Project Regional Experiment (FIRE) data described in Moeng et al. (1996). The second one is a low cloud cover, trade wind cumulus case based on the Barbados Oceanographic and Meteorological Experiment (BOMEX) from Siebesma et al. (2003). The third case is derived from observations made at the Southern Great Plains (SGP) site of the Atmospheric Radiation Measurement (ARM) Program on 21 June 1997

(Brown et al., 2002) and focuses on the development of shallow cumulus clouds over land. Finally, the fourth case consists of trade wind cumulus clouds under a strong inversion with the development of a stratiform cloud at the top of the cloud layer (Stevens et al., 2001). The large-scale conditions for the latter case are derived from observations collected during the Atlantic Trade Wind Experiment (ATEX).

COAMPS-LES has been set up for each case by following the intercomparison guidelines as closely as feasible. A summary of the model configuration is given in Table I. Two simulations are performed for each case, one with the TKE subgrid model and one with the Lilly–Smagorinsky model (hereafter referred to as TKE and L–S experiments). As mentioned above, the dynamics variables are integrated using a leapfrog time step and a centred second-order advection. Both a fourth-order numerical diffusion with coefficient  $\nu = 0.001$  and a Robert filter with coefficient 0.2 are applied to the leapfrog variables. The thermodynamics variables use a forward time step and the Bott advection with second-order polynomial interpolation. The specifications for the FIRE case do not call for a specific longwave radiation scheme. For this case, we therefore used the same simplified scheme as recommended for the ATEX case.

In the following subsections, we present selected results from the COAMPS-LES and compare them with the published results of other LES models.

### 3.1. FIRE NOCTURNAL STRATOCUMULUS CASE

Figure 1 shows the time evolution of domain averaged cloud-top height, cloud cover, liquid water path (LWP), and vertically averaged TKE during the first 2 h of the FIRE case. Cloud cover is defined as the fraction of model column with liquid water anywhere in the column. The TKE and L–S experiments exhibit only small differences. Compared to the other models, COAMPS-LES is within the overall model variability.

Vertical profiles of selected quantities averaged over the second hour of the simulation are plotted in Figure 2. Again, the differences between the TKE and

TABLE I

Summary of grid size, horizontal and vertical grid increment, time step and simulation length for the four different experiments.

Experiment	Grid size	$\Delta x, \Delta y$ (m)	$\Delta z$ (m)	$\Delta t$ (s)	Length (hour)
FIRE	$64 \times 64 \times 48$	50	25	1.5	2
BOMEX	$4 \times 64 \times 75$	100	40	1.5	6
ARM	$67 \times 67 \times 110$	100	40	1.0	14.5
ATEX	$64 \times 64 \times 150$	100	20	1.0	8

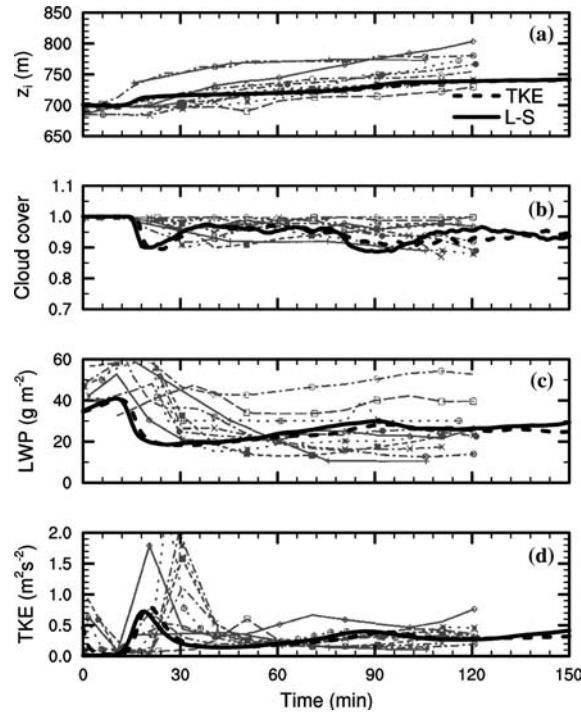


Figure 1. Time evolution from the FIRE case: (a) average cloud-top height, (b) cloud cover, (c) liquid water path, and (d) TKE averaged over the PBL. Thick solid line is the Lilly-Smagorinsky simulation and thick dashed line the TKE simulation. Thin light lines are results from other LES models (Moeng et al., 1996, Figure 3).

L-S experiments are negligible and the COAMPS-LES results lie within the range given by the other models. The predicted boundary-layer depth is 720 m and the boundary layer is well mixed due to the cloud-top radiative cooling. The maximum cloud liquid water predicted by the COAMPS-LES is just under  $0.2 \text{ g kg}^{-1}$ , which puts it almost in the middle of the range of the other LESs. Profiles of the turbulent fluxes are fairly typical for a stratocumulus layer.

### 3.2. BOMEX TRADE WIND CUMULUS CASE

The time evolution of cloud cover, liquid water path, and vertically integrated TKE for the BOMEX case is shown in Figure 3. The COAMPS-LES results have not been time filtered and therefore show considerably more intermittency than the mean of the other models. COAMPS-LES cloud cover is slightly smaller than the mean, but the LWP and integrated TKE are comparable.

Profiles averaged over the last 3 h are depicted in Figure 4. There are no discernible differences between COAMPS-LES and the other models for the potential temperature and water vapour mixing ratio. A slight difference can be seen in the  $u$  and  $v$  winds in the subcloud layer. The liquid water mixing ratio

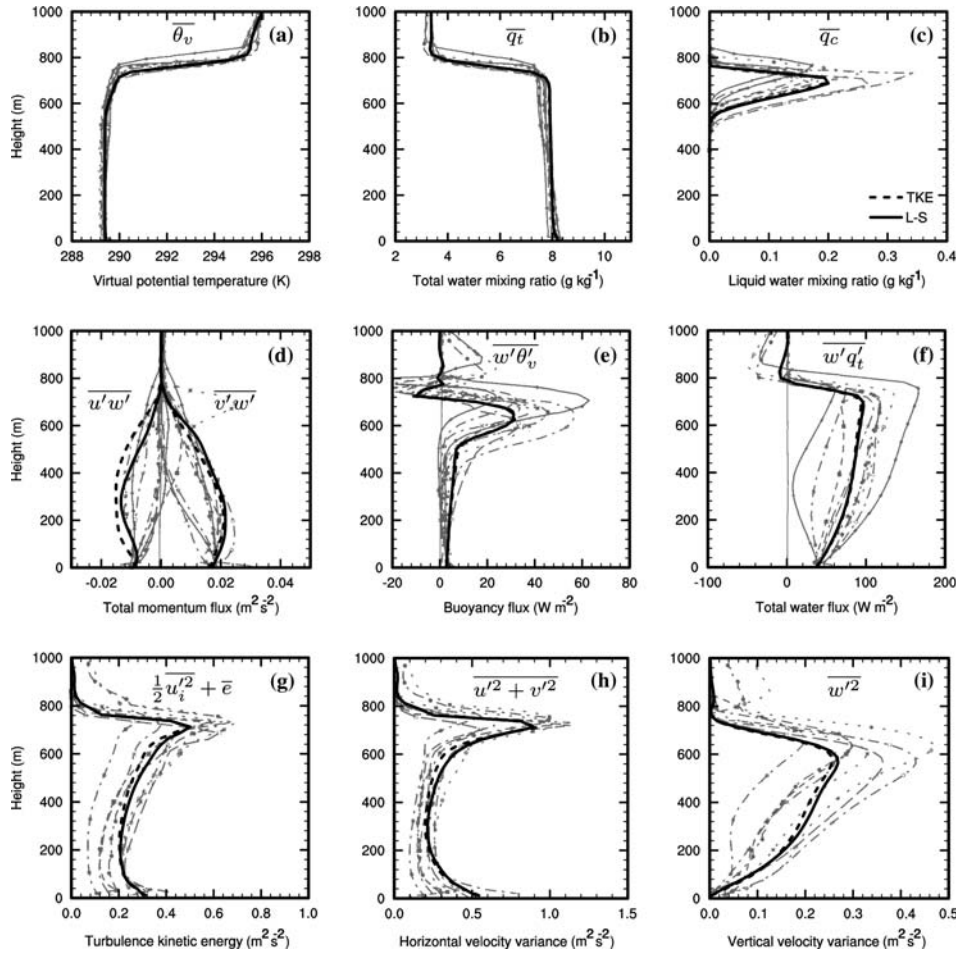


Figure 2. Vertical profiles averaged over the second hour of the FIRE case: (a) virtual potential temperature, (b) total water mixing ratio, (c) liquid water mixing ratio, (d)  $u$  and  $v$  momentum fluxes, (e) buoyancy flux, (f) total water flux, (g) total TKE, (h) resolved horizontal velocity variance, (i) resolved vertical velocity variance. Lines follow same convention as the previous figure (Moeng et al., 1996, Figures 5, 6, 7).

reveals small differences between the TKE and L-S experiments. The L-S experiment has more cloud water compared to the TKE one, but both produce a cloud field within the standard deviation of the other models.

Finally, Figure 5 shows some of the turbulent moments. The overall agreement with other models is good, and only minor differences can be seen between the TKE and L-S simulations. The TKE experiment tends to have smaller turbulent moments in the cloud layer, consistent with its less vigorous cloud field. The total water flux (Figure 5a) in the subcloud layer of the COAMPS-LES experiments indicates a drying at odds with the predicted moistening from the other models. However, it appears to be small enough to

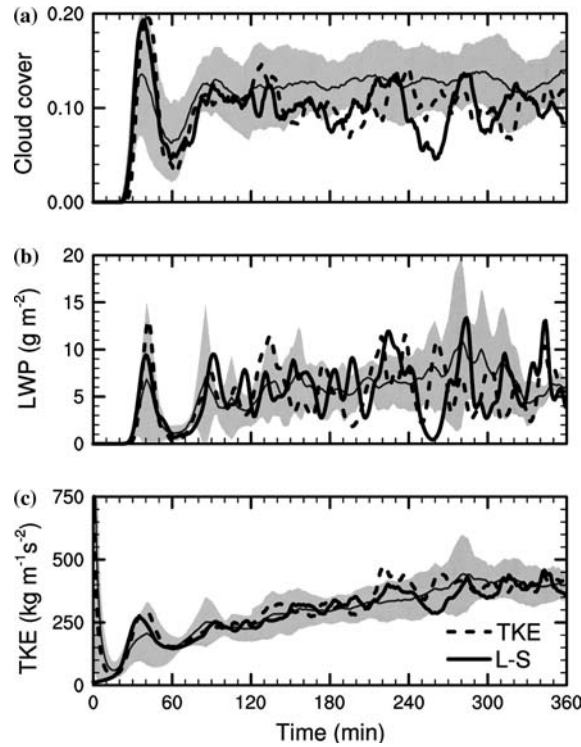


Figure 3. Time evolution from the BOMEX case: (a) cloud cover, (b) liquid water path, and (c) vertically integrated TKE. Thick solid line is the Lilly-Smagorinsky simulation and thick dashed line the TKE simulation. Thin solid line is average and shaded band is twice the standard deviation of other LES models (Siebesma et al., 2003, Figure 2).

not translate into a noticeable difference in the mean water vapour profile (Figure 4b).

### 3.3. ARM SHALLOW CUMULUS OVER LAND

One major difference between the ARM and the BOMEX cases is the presence of the land surface, which results in a large diurnal cycle in the surface heat fluxes. For intercomparison purposes, the presence of the land surface is mimicked by imposing time varying surface fluxes that approximately correspond to observations collected at the SGP ARM site (Brown et al., 2002). The first clouds form approximately 4 h after the beginning of the simulation and deepen throughout the day. Cloud cover reaches its peak value 3 h after the formation of the first clouds. Figure 6 shows the time evolution of the total cloud cover, the maximum cloud fraction, and the domain cloud-base and cloud-top heights. The TKE and L-S experiments produce comparable evolutions that agree well with the other models. Other aspects of the COAMPS-LES results for this shallow cumulus case over land are also in good agreement.

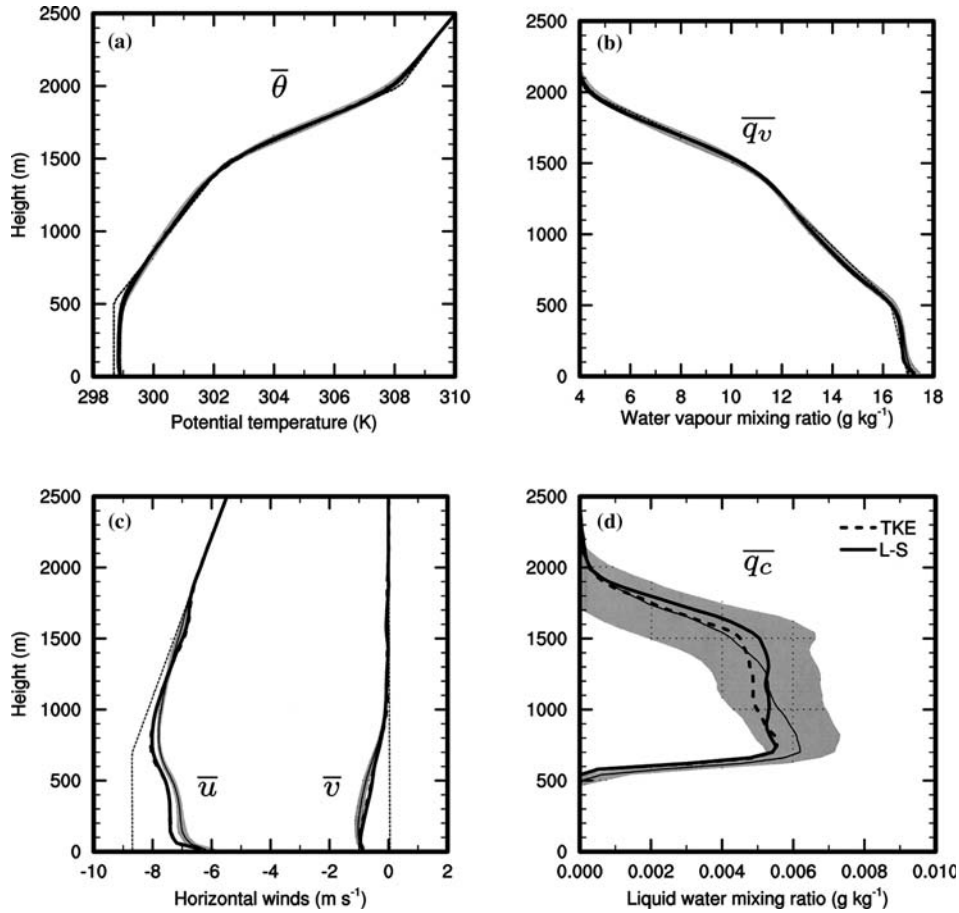


Figure 4. Vertical profiles averaged over the last 3 h of the BOMEX case: (a) potential temperature, (b) water vapour mixing ratio, (c) horizontal winds, and (d) liquid water mixing ratio. Lines follow same convention as the previous figure. The thin dashed lines in panels (a), (b) and (c) indicate the initial profiles. (Siebesma et al., 2003, Figure 3).

### 3.4. ATEX TRADE WIND CUMULI UNDER A STRONG INVERSION

Time evolution of selected variables during the 8 h of the ATEX experiment is shown in Figure 7. COAMPS-LES surface latent and sensible heat fluxes (Figure 7a, e) compare very well to the mean of the other models. Cloud properties, such as cloud cover and domain-averaged LWP, reveal that COAMPS-LES produces more clouds on average. The cloud cover (Figure 7b) reaches 80% for the TKE and 70% for the L-S experiment, compared to 50% for the average, reflecting an anvil with greater aerial coverage. The LWP path is also larger, although it falls at most times within one standard deviation of the other models (Figure 7d). The greater

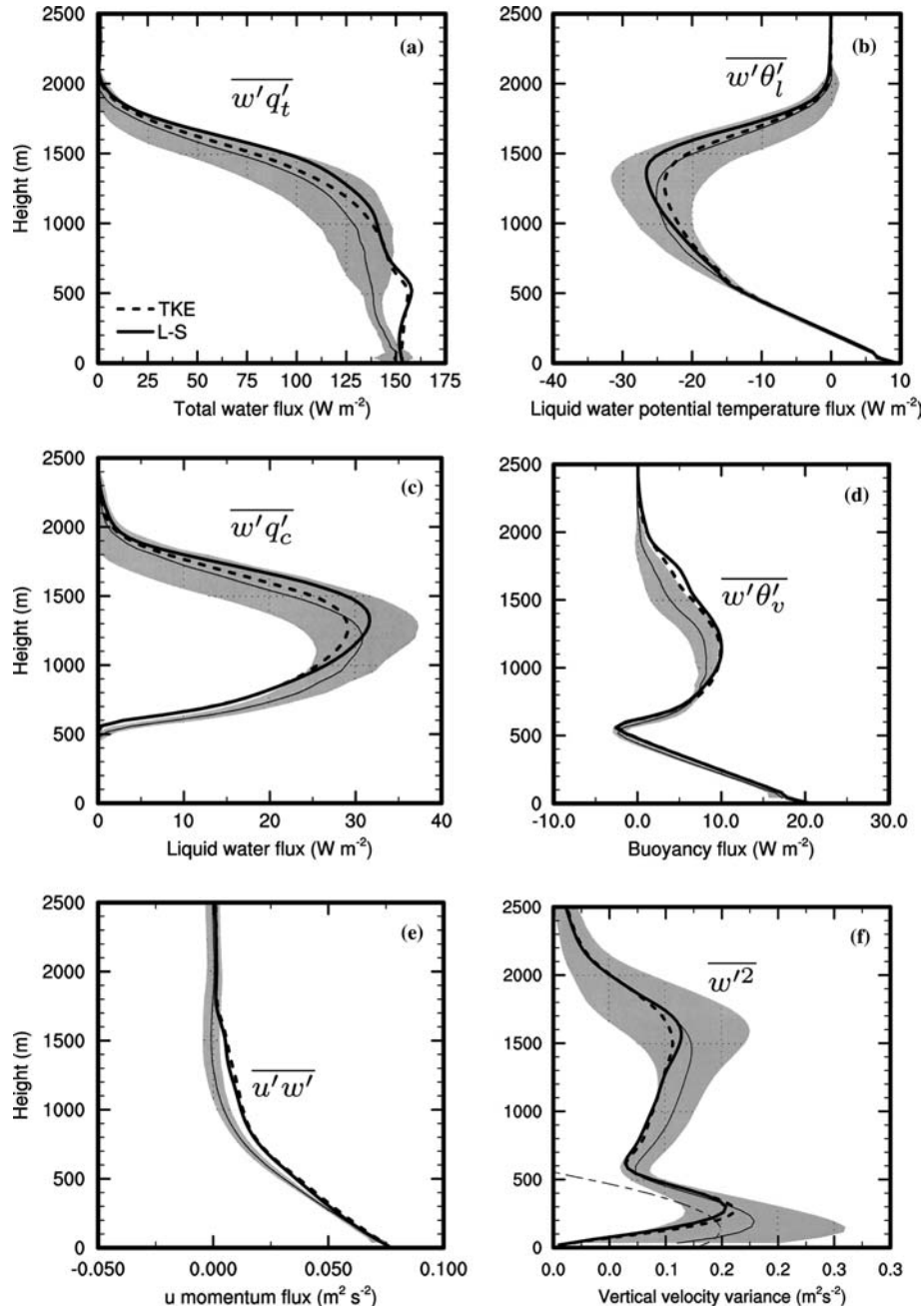


Figure 5. Vertical profiles averaged over the last 3 h of the BOMEX case: (a) total water flux, (b) liquid water potential temperature flux, (c) liquid water flux, (d) buoyancy flux, (e)  $u$  momentum flux, and (f) vertical velocity variance. Lines follow same convention as the previous figure. The thin dashed line in (f) corresponds to the mixed-layer scaling (Siebesma et al., 2003, Figures 4 and 5).

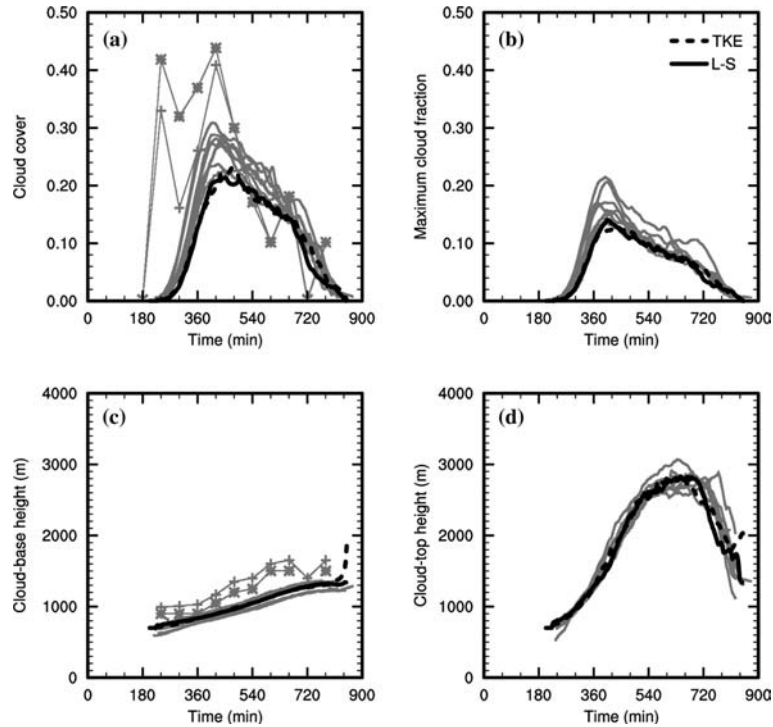


Figure 6. Time evolution (smoothed over one hour) from the ARM case: (a) cloud cover, (b) maximum cloud fraction at any one level, (c) cloud-base height, and (d) cloud-top height. Thick lines are COAMPS-LES results for L-S and TKE experiments, light lines are results from other LESs. In (a) and (c), the stars and crosses are lidar and ceilometer observations (Brown et al., 2002, Figure 5).

anvil translates into larger cloud-top radiative cooling and in turn into more vigorous turbulence mixing, especially for the last 3 h (Figure 7c). The overall entrainment velocity is in line with the other models (Figure 7f).

Vertical profiles are plotted in Figure 8. The relatively larger cloud-top anvil can be seen from the liquid water mixing ratio profile (Figure 8a). The average of the other models yields a liquid water mixing ratio of  $0.06 \text{ g kg}^{-1}$  at cloud top; L-S produces 0.1 and TKE  $0.125 \text{ g kg}^{-1}$ , this latter value being just above the standard deviation of the other models. However, despite these cloud anvil differences, the profiles of total water mixing ratio (Figure 8a) and potential temperature (Figure 8b) are very close to the other models. Horizontal winds are slightly off compared to the average (Figures 8c, d). Turbulent fluxes (Figure 8e–h) are all within the standard deviation of the other LESs.

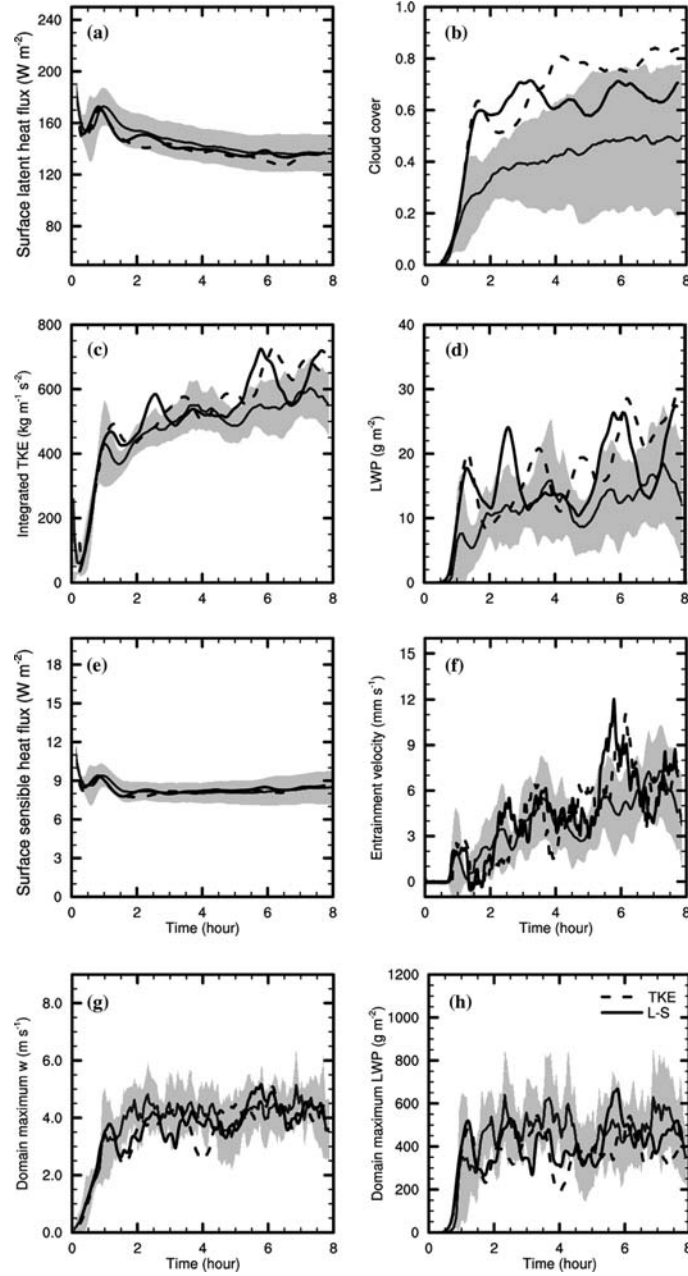


Figure 7. Time evolution (smoothed over 30 min) from the ATEX case: (a) surface latent heat flux, (b) cloud cover, (c) vertically integrated TKE, (d) liquid water path, (e) surface sensible heat flux, (f) mean vertical velocity of  $q_l = 6.5 \text{ g kg}^{-1}$  contour, (g) maximum vertical velocity in the domain, and (h) maximum liquid water path in a model column. Thick lines are COAMPS-LES results for L-S and TKE experiments, thin solid line is average and shaded region is twice the standard deviation of other LES models (Stevens et al., 2001, Figure 2).

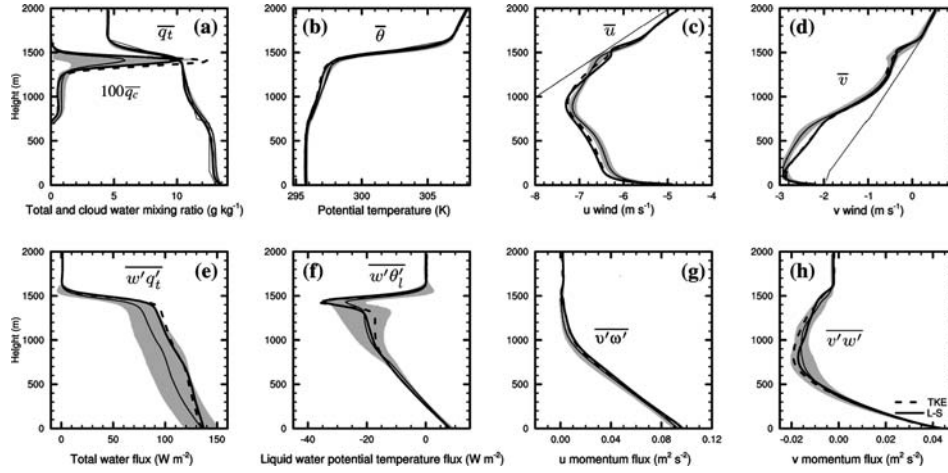


Figure 8. Vertical profiles averaged over the last 5 h of the ATEX case: (a) total water and liquid water mixing ratios, (b) potential temperature, (c)  $u$  wind, (d)  $v$  wind, (e) total water flux, (f) liquid water potential temperature flux, (g)  $u$  momentum flux, and (h)  $v$  momentum flux. Lines follow same convention as the previous figure (Stevens et al., 2001, Figure 3).

### 3.5. SUMMARY

We believe that the above mentioned results serve as a validation of the LES extensions to COAMPS. The model numerical components were identically configured for all experiments with no case specific switches used. Our results are also quite insensitive to the choice of L-S or TKE subgrid model, which is desirable (Mason, 1994). Overall, COAMPS-LES results are in very good agreements with other models.

Using COAMPS-LES, we have also successfully participated in two recent intercomparison studies: a stable boundary-layer case (Beare et al., 2005) and a stratocumulus case based on the first research flight of the second Dynamics and Chemistry of Marine Stratocumulus field study (Stevens et al., 2003, DYCOMS-II). Description of LES results for this latter case is the subject of a separate publication (Stevens et al. 2005).

## 4. Higher Moment Vertical Velocity Budgets

Governing equations for the second and third moments of the vertical velocity are traditionally derived from the  $w$  momentum equation using the Reynolds rules of averaging in conjunction with incompressibility and horizontal homogeneity assumptions (e.g. Stull, 1988; André et al., 1976):

$$\frac{\partial \overline{w'^2}}{\partial t} = -\overline{w} \frac{\partial \overline{w'^2}}{\partial z} - \frac{\partial \overline{w'^3}}{\partial z} - 2\overline{w'^2} \frac{\partial \overline{w}}{\partial z} + \frac{2g}{\theta_0} \overline{w' \theta'_v} - \frac{2}{\rho_0} \overline{w' \frac{\partial p'}{\partial z}} - \epsilon_{www} \quad (24)$$

Advection                      Buoyancy      Pressure      Dissipation

$$\frac{\partial \overline{w'^3}}{\partial t} = -\overline{w} \frac{\partial \overline{w'^3}}{\partial z} - \frac{\partial \overline{w'^4}}{\partial z} + 3\overline{w'^2} \frac{\partial \overline{w}}{\partial z} - 3\overline{w'^3} \frac{\partial \overline{w}}{\partial z} + \frac{3g}{\theta_0} \overline{w'^2 \theta'_v} - \frac{3}{\rho_0} \overline{w'^2 \frac{\partial p'}{\partial z}} - \epsilon_{www} \quad (25)$$

Advection                      Buoyancy  
Pressure                      Dissipation

Because of the incompressibility assumption, these equations are not strictly valid for COAMPS-LES. However, they do provide useful guidance in interpreting budget terms. Budgets for the higher moments from numerical models are sometimes constructed by computing a number of terms appearing in Equations (24)–(25) directly from the model fields, while inferring the remaining ones using a residual approach. This approach does not guarantee complete accuracy and consistency of the budget. Therefore, we prefer to follow an alternate approach in which we first construct an exact numerical budget (within machine precision) from the model numerical code, and then relate the various contributions of that budget to terms appearing in Equations (24)–(25).

Details on how we obtain exact numerical budgets are given in the Appendix. These budgets provide contributions from the advection, buoyancy, pressure and dissipation terms; the effect of the Robert time filter is folded in the dissipation term. The  $\overline{w'^3}$  budget contains an additional residual term arising from non-linear interactions between processes.

#### 4.1. COMPARISONS OF $\overline{w'^2}$ , $\overline{w'^3}$ , $Sk_w$

First, we compare vertical profiles of domain-averaged resolved  $\overline{w'^2}$ ,  $\overline{w'^3}$  and skewness  $Sk_w \equiv \overline{w'^3} / \overline{w'^2}^{3/2}$  for FIRE, BOMEX and ATEX (Figure 9). ARM case profiles are qualitatively similar to BOMEX and are therefore not shown. All profiles are from the experiments using the L–S subgrid-scale scheme, although our discussion would be equally applicable to the TKE experiments. Broadly speaking,  $\overline{w'^2}$  can be interpreted as a measure of the intensity of the turbulence, whereas  $\overline{w'^3}$  provides additional information about its organization. Small values of  $\overline{w'^3}$  occur when the distribution of  $w$  is relatively symmetric between updraughts and downdraughts regardless of the

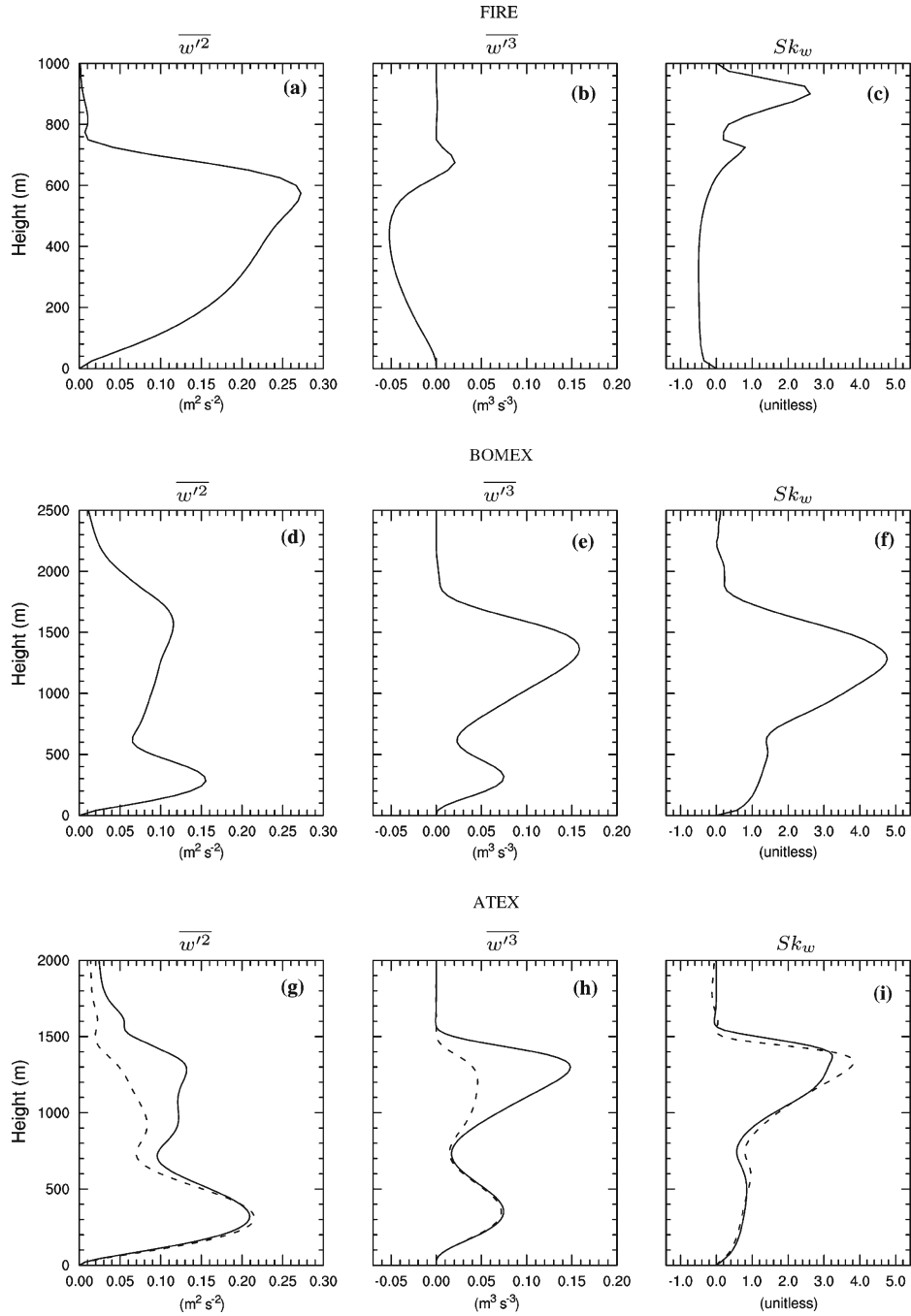


Figure 9. Vertical profiles of resolved  $\overline{w'^2}$ ,  $\overline{w'^3}$  and skewness ( $Sk_w$ ) averaged over their respective analysis time period for the FIRE, BOMEX and ATEX experiments using the L-S subgrid-scale scheme. The dashed line in panels g, h, and i are for the ATEX sensitivity experiment in which cloud-top radiative cooling was turned off.

strength of the turbulence. Large positive values of  $\overline{w'^3}$  indicate the dominance of strong and narrow updraughts, and large negative values indicate strong and narrow downdraughts. The skewness  $Sk_w$  is essentially a normalised measure of  $\overline{w'^3}$ .

The nature of the mixing is very different between FIRE and BOMEX. Turbulent motions in the FIRE case are generated by cloud-top radiative cooling. In BOMEX, they are generated by surface fluxes and conditional instability that lead to the formation of shallow cumulus clouds. This translates into markedly different  $w$  moments as shown in Figure 9. The strength of the turbulence as measured by  $\overline{w'^2}$  is greater for FIRE than BOMEX. The FIRE  $\overline{w'^2}$  profile shows a single maximum in the cloud. In contrast, the profile from BOMEX exhibits one local maximum in the sub-cloud layer related to the eddies generated from the surface fluxes, and a second maximum in the cloud layer due to latent heat release.

Profiles of  $\overline{w'^3}$  and  $Sk_w$  show an almost unskewed turbulent field for FIRE. The skewness has a nearly constant value of  $-0.5$  in the lower portion of the mixed layer and a small positive maximum near cloud top. The larger maximum around 900 m is caused by small  $\overline{w'^2}$  values in the denominator of  $Sk_w$  and has little physical relevance. The negative skewness in the mixed layer indicates slightly stronger and narrower downdraughts, which is consistent with cloud-top radiatively driven turbulence.

A different picture emerges for BOMEX;  $\overline{w'^3}$  and the skewness are positive throughout the entire boundary layer. The skewness reaches a large maximum of nearly 5 in the upper portion of the cloud layer. The cloud layer increase in skewness can be interpreted as updraughts becoming progressively stronger and narrower with height in accordance with the cloud core analysis of Siebesma et al. (2003, Figures 6 and 10).

Despite significant differences in cloud fields between BOMEX and ATEX, Figure 9 reveals that the ATEX  $w$  moments resemble BOMEX much more closely than FIRE, thus suggesting that the turbulence organization is dominated by the shallow cumulus clouds. To verify this, we have performed a sensitivity ATEX experiment in which the longwave cloud-top cooling was removed. This experiment resulted in smaller values of cloud fraction and liquid water near the inversion, but comparable amounts in the underlying cumulus layer. The  $w$  moments from the sensitivity experiment are displayed in Figures 9g–i using a dashed line. Compared to the reference ATEX simulation,  $\overline{w'^2}$  and  $\overline{w'^3}$  are almost identical in the subcloud layer, but become much smaller in the cloud layer. Remarkably, the skewness profiles are almost identical between the two experiments. Therefore, even though the level of turbulence activity is considerably affected by the presence or the absence of cloud-top radiative cooling, the asymmetry between updraughts and downdraughts is not. Because of the similarity between BOMEX and ATEX

with respect to the  $w$  moments, we limit our presentation of higher moment budgets to the FIRE and BOMEX experiments.

It is also noteworthy to point out that, for both BOMEX and ATEX,  $\overline{w'^2}$  extends to higher levels than  $\overline{w'^3}$ . The motions in the layer above cloud top where  $\overline{w'^2}$  is positive but  $\overline{w'^3}$  is almost zero are likely dominated by wave activity (Cuijpers et al., 1996).

#### 4.2. $\overline{w'^2}$ BUDGETS

The  $\overline{w'^2}$  budget for FIRE is shown in Figure 10. Terms shown are advection, buoyancy, pressure, dissipation, and storage (actual model change during the analysis time period). The net term (difference between the sum of all the terms and the storage) is essentially zero as can be seen from the vertically integrated contribution of each budget term in Table II. Also shown with the advection term is the resolved turbulent transport term as computed from the model field ( $-\partial \overline{w'^3}/\partial z$ ). The buoyancy term is decomposed into contributions from updraughts and downdraughts:

$$\overline{w'\theta'_v} = a\overline{w'\theta'_v}^u + (1-a)\overline{w'\theta'_v}^d \quad (26)$$

where  $a$  is the updraught area and  $(\overline{\quad})^u, (\overline{\quad})^d$  denote averages over the updraught, respectively downdraught, portion of the flow. This simple decomposition is exact and can be useful in interpreting the role of buoyancy. For example, warm updraughts ( $w'_u > 0, \theta'_{u,v} > 0$ ) and cold downdraughts ( $w'_d < 0, \theta'_{d,v} < 0$ ) can both contribute positively to the buoyancy. Wang and Stevens (2000) performed a more sophisticated decomposition and showed that a properly chosen conditional sampling could explain a large portion of the fluxes but failed to explain the variances for both cumulus and stratocumulus clouds.

The  $\overline{w'^2}$  budget is in many respects similar to budgets analysed by Moeng (1986, Figure 19) for two stratus-topped boundary layers. The major terms are buoyancy, pressure and advection. The buoyancy acts as a source of turbulence throughout the boundary layer with the exception of the entrainment zone. The buoyancy flux decomposition reveals that both updraught and downdraught contributions are positive throughout most of the boundary layer. This can occur when the perturbation virtual potential temperature is positive in updraughts ( $w'_u > 0, \theta'_{v,u} > 0$ ) and negative in downdraughts ( $w'_d < 0, \theta'_{v,d} < 0$ ). Furthermore, updraughts and downdraughts contribute nearly equally to the generation of turbulence, except in the entrainment zone. In this region, the updraughts are negatively buoyant and buoyancy becomes a sink of energy, whereas downdraughts do not contribute significantly.

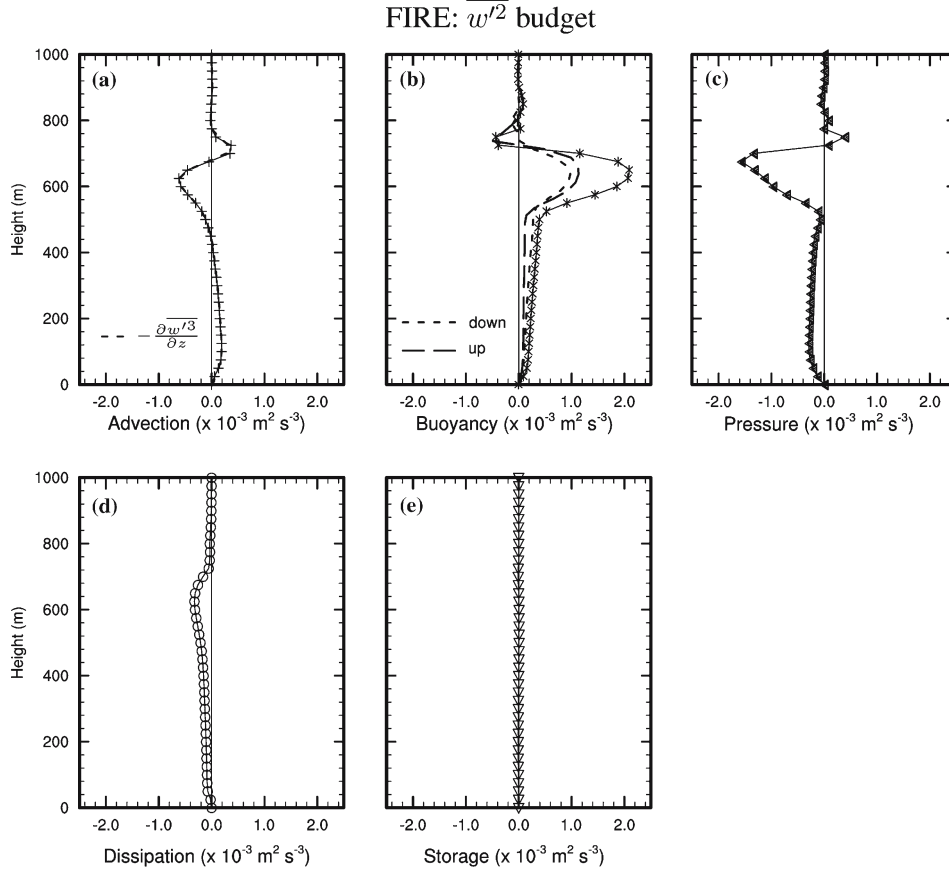


Figure 10.  $\overline{w'^2}$  budget terms for the FIRE experiment with L-S subgrid-scale scheme: (a) advection term (line with crosses) and estimated transport term  $-\partial \overline{w'^3} / \partial z$  (dashed line), (b) buoyancy term (line with stars), updraughts (long dashed line) and downdraughts (short dashed line) contributions to the buoyancy, (c) pressure term, (d) dissipation term, (e) storage. The net term (not shown) is negligible.

The pressure term (Figure 10c) is the largest sink of  $\overline{w'^2}$ , and redistributes energy from the vertical to the horizontal directions. It peaks just below cloud top where updraughts are impeded in their ascent by the presence of the inversion and as a result have their momentum diverted in the horizontal. The advection term and the turbulent transport term  $-\partial \overline{w'^3} / \partial z$  computed directly from the model fields show no visible differences (Figure 10a). This term transports  $\overline{w'^2}$  from the cloud layer into both the entrainment zone and the subcloud layer. The dissipation term is comparatively small in magnitude. It acts to dissipate  $\overline{w'^2}$  and peaks in the cloud layer. Its influence on our budget appears to be smaller than the dissipation term of Moeng (1986).

However, its quantitative contribution, as shown by the vertically integrated budget (Table II), is not negligible.

The corresponding  $\overline{w'^2}$  budget for BOMEX is depicted in Figure 11. It compares favourably with similar budgets from other shallow cumulus simulations discussed by Cuijpers et al. (1996, Figure 12) and de Roode and Bretherton (2003, Figure 1). As for FIRE, buoyancy is the major source of kinetic energy, except in a shallow region near cloud base where subcloud driven updraughts decelerate before undergoing renewed acceleration due to latent heat release in the cloud. The updraught and downdraught decomposition reveals that the buoyancy production is largely dominated by the updraughts from the surface up to 1600 m ( $w'_u > 0$ ,  $\theta'_{v,u} > 0$ ). Between 1700 m and the domain cloud top, updraughts become negatively buoyant ( $w'_u > 0$ ,  $\theta'_{v,u} < 0$ ), and consume their kinetic energy by overshooting into the inversion layer. The generation of turbulence in this layer is dominated by the downdraughts ( $w'_d < 0$ ,  $\theta'_{v,d} < 0$ ) forced by evaporative cooling. In contrast to FIRE, the pressure and dissipation terms have comparable magnitudes. Because of the absence of a very strong inversion, there is less redistribution of energy from the vertical to the horizontal motions by the pressure term. The advection term is also relatively large. It mainly acts by transporting energy from the lower half to the upper half of the subcloud layer, and again from the lower portion to the upper portion of the cloud layer.

Some interesting differences emerge from the FIRE and BOMEX  $\overline{w'^2}$  budgets. Although buoyancy is the source of turbulence in both cases, its shape and vertical distribution are quite different. This is not surprising given the fundamentally different nature of the turbulence. For the radi-

TABLE II  
Vertically integrated contributions from the various  $\overline{w'^2}$  and  $\overline{w'^3}$  budget terms for the FIRE and BOMEX experiments using the L-S subgrid-scale scheme.

	FIRE		BOMEX	
	$\overline{w'^2}(\times 10^{-3} \text{ m}^3 \text{ s}^{-3})$	$\overline{w'^3}(\times 10^{-3} \text{ m}^4 \text{ s}^{-4})$	$\overline{w'^2}(\times 10^{-3} \text{ m}^3 \text{ s}^{-3})$	$\overline{w'^3}(\times 10^{-3} \text{ m}^4 \text{ s}^{-4})$
Advection	-1.33	44.91	13.41	273.62
Buoyancy	415.15	-33.03	775.44	1649.92
Pressure	-292.28	-42.18	-370.27	-989.01
Dissipation	-120.22	34.56	-418.39	-947.68
Residual		-1.36		-0.65
Storage	-1.32	-2.90	-0.19	13.80
Net	0.00	0.00	0.00	0.00

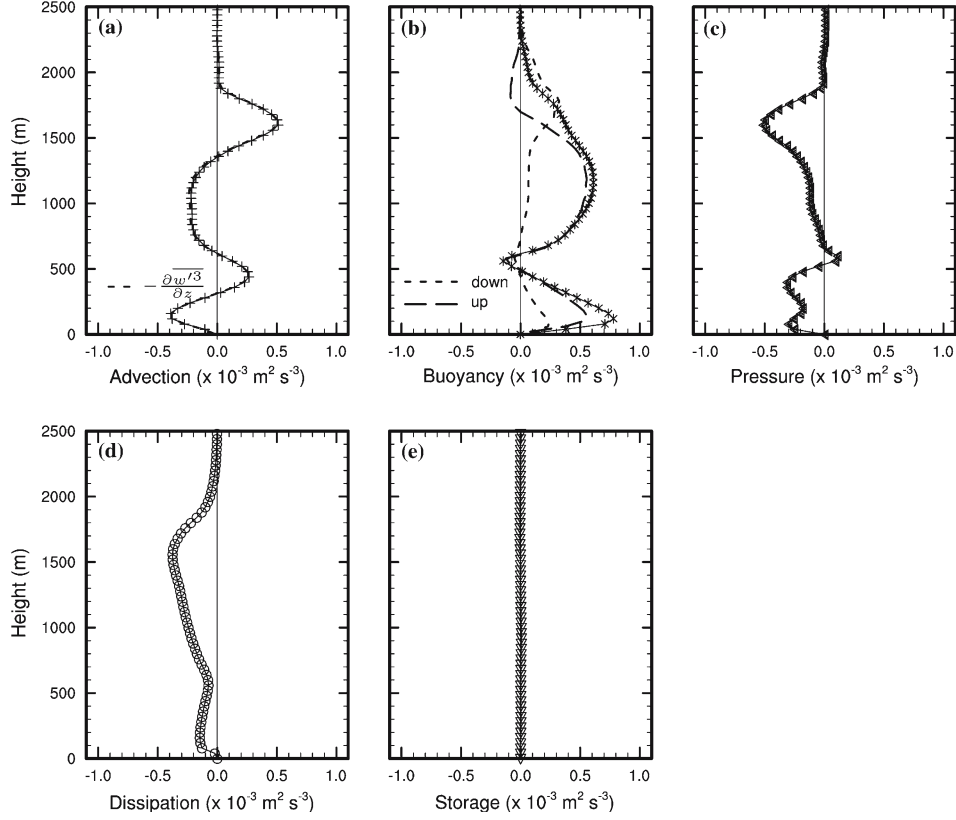
BOMEX:  $\overline{w'^2}$  budget

Figure 11. Same as Figure 10 but for the BOMEX experiment with the L-S subgrid-scale scheme.

actively driven cloud-top turbulence, both updraughts and downdraughts contribute to the generation of buoyancy throughout the entire mixed layer, except in the entrainment zone where updraughts dominate. In contrast, for the shallow cumulus convection, the updraughts are almost the exclusive source of buoyancy from the surface up to the level of neutral buoyancy. Above that level, evaporative cooling generates downdraughts, which act as primary source of buoyancy. The pressure term dissipates  $\overline{w'^2}$  by redistributing kinetic energy from the vertical to the horizontal in both cases. However, the magnitude of this redistribution is much larger in the stratocumulus compared to the cumulus case due to the presence of a strong inversion.

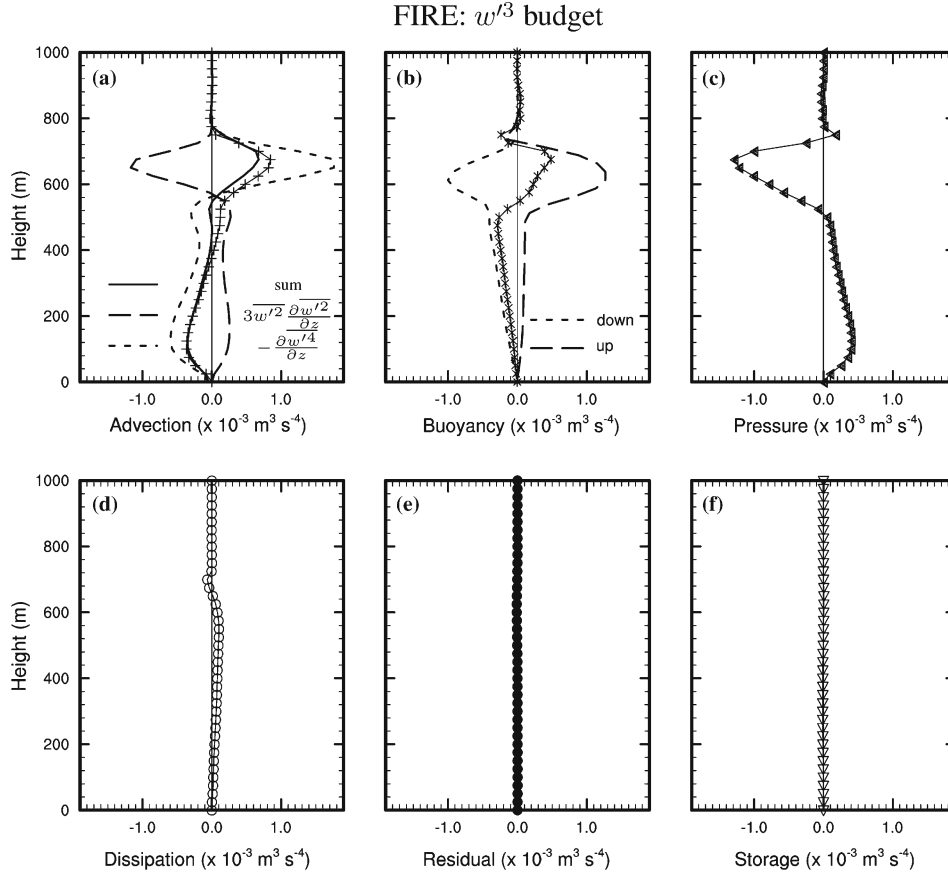


Figure 12.  $\overline{w'^3}$  budget terms for the FIRE experiment with L-S subgrid-scale scheme: (a) advection term (line with crosses), estimated transport term  $-\partial \overline{w'^4}/\partial z$  (short dashed line), estimated turbulent production term  $3\overline{w'^2} \partial \overline{w'^2}/\partial z$  (long dashed line) and their sum (solid line), (b) buoyancy term (line with stars), updraughts (long dashed line) and downdraughts (short dashed line) contributions to the buoyancy, (c) pressure term, (d) dissipation term, (e) residual term arising from the non-linear interactions between budget terms, (f) storage. The net term (not shown) is negligible.

#### 4.3. $\overline{w'^3}$ BUDGETS

The FIRE  $\overline{w'^3}$  budget is plotted in Figure 12. Terms shown are the advection, buoyancy, pressure, dissipation, residual (non-linear interactions between budget terms, last term on RHS of Equation (A12)) and storage. The net term is negligible. The vertically integrated contributions from all the terms are given in Table II. Shown along with the advection are two terms computed directly from Equation (25): the turbulence advection ( $-\partial \overline{w'^4}/\partial z$ ) and turbulence production ( $3\overline{w'^2} \partial \overline{w'^2}/\partial z$ ). The buoyancy is again decomposed into updraught and downdraught contributions:

$$\overline{w'^2\theta'_v} = a\overline{w'^2\theta'_v}^u + (1-a)\overline{w'^2\theta'_v}^d. \quad (27)$$

In contrast to Equation (29), the sign of  $\overline{w'^2\theta'_v}^u$  and  $\overline{w'^2\theta'_v}^d$  is essentially governed by the sign of the temperature perturbations ( $\theta'_{v,u}$ ,  $\theta'_{v,d}$ ), but the magnitude is influenced by the strength of the turbulence ( $w'^2_u$  and  $w'^2_d$ ).

The largest terms in the FIRE budget are advection, buoyancy and pressure. The buoyancy, which consists of a positive contribution from the updraughts and a negative one from the downdraughts, changes sign at 580 m corresponding approximately to cloud base. The negatively buoyant downdraughts ( $w'^2_d > 0$ ,  $\theta'_{v,d} < 0$ ) generated by cloud-top cooling dominate the buoyancy below cloud base, whereas the latent heat release in the updraughts is dominant inside the cloud layer ( $w'^2_u > 0$ ,  $\theta'_{v,u} > 0$ ). The pressure term acts to dissipate  $\overline{w'^3}$  except in a shallow layer between cloud base (580 m) and 620 m where  $\overline{w'^3}$  and the pressure term have the same sign.

The sum of the estimated contribution from the turbulent transport term ( $-\partial\overline{w'^4}/\partial z$ ) and the mean  $\overline{w'^2}$  gradient production term ( $3\overline{w'^2}\partial\overline{w'^2}/\partial z$ ) matches the advection term very well in the subcloud layer, but is slightly smaller in the cloud layer (Figure 12 a). This could be due to the fact that these terms do not correspond exactly to the transport and production terms “seen” by the model due to numerical finite difference approximations. Nevertheless, the sum is close enough for the decomposition to be meaningful. It reveals that turbulence transports  $\overline{w'^3}$  from the subcloud to the cloud layer and is countered by the production term, which has the opposite sign. The dissipation term in the budget has a smaller magnitude, although its vertically integrated contribution is not negligible (Table II).

Figure 13 shows the  $\overline{w'^3}$  budget for BOMEX. Cuijpers et al. (1996, Figure 13) analysed a  $\overline{w'^3}$  budget from another simulation of shallow cumulus clouds, which shows similar characteristics to ours. In contrast to FIRE, the BOMEX  $\overline{w'^3}$  budget is dominated by production due to buoyancy. Between the surface and 1700 m, the buoyancy term consists almost exclusively of contributions from the updraughts, and above that level the situation is reversed. Downdraughts generated by evaporative cooling in the inversion layer account for most of the buoyancy term there. The partitioning between updraughts and downdraughts contributions is quite similar to the  $\overline{w'^2}$  buoyancy term (Figure 11b). The advection term is dominated by the turbulence transport term ( $-\partial\overline{w'^4}/\partial z$ ), which transports ( $\overline{w'^3}$ ) from the lower portion to the upper portion of the cloud layer. The production term  $3\overline{w'^2}\partial\overline{w'^2}/\partial z$  only plays a minor role in the subcloud layer. Pressure and dissipation act to dissipate  $\overline{w'^3}$  and tend to be largest near the top of the cloud layer.

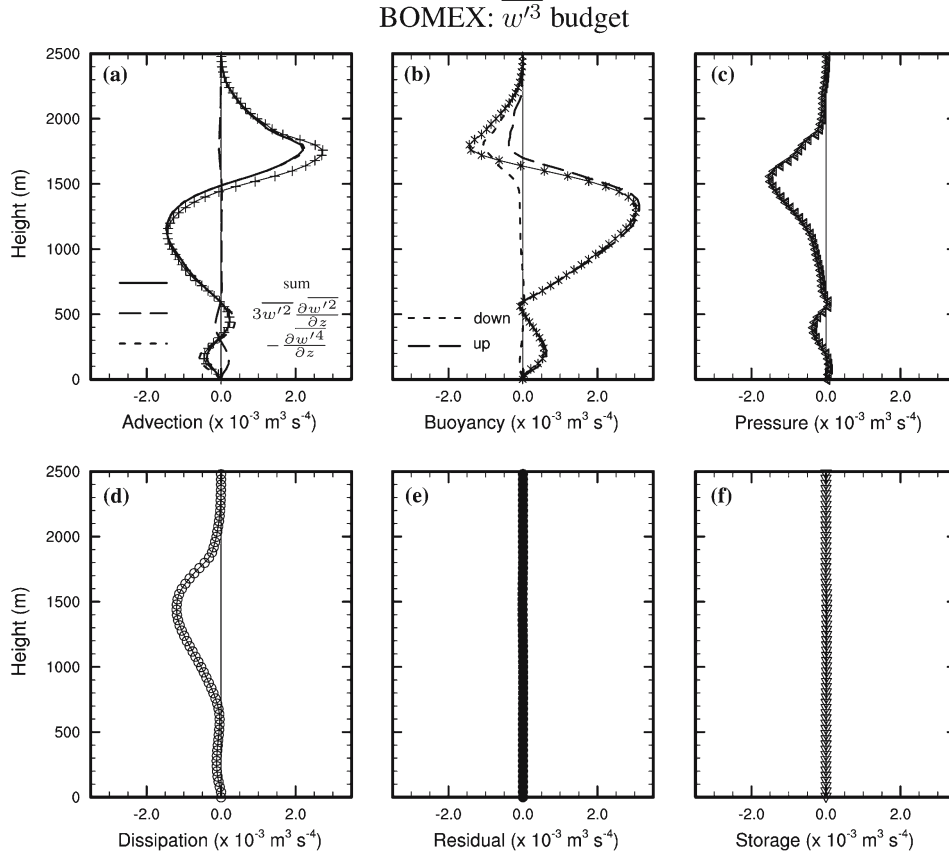


Figure 13. Same as Figure 12 but for the BOMEX experiment with the L-S subgrid-scale scheme.

Comparisons of the  $\overline{w'^3}$  budgets for FIRE and BOMEX reveal interesting differences. Buoyancy is dominant in BOMEX and plays a more modest role in FIRE. In BOMEX buoyancy is itself dominated by contributions from updraughts except in the inversion layer where the downdraughts generated by evaporative cooling take over. However, in FIRE, both updraughts and downdraughts have comparable contributions but of opposite signs throughout the depth of the boundary-layer. This competition between a positive contribution from updraughts and negative one from the downdraughts explains in large part why  $\overline{w'^3}$  and  $Sk_w$  are much smaller for FIRE than BOMEX.

## 5. Conclusion

COAMPS has been successfully extended to perform as a LES model by implementing two new LES subgrid model options. They consist of a Lilly–Smagorinsky local equilibrium and a TKE scheme. The extended model has been validated using four intercomparison case studies of boundary-layer cloud regimes for which extensive comparison with published results is possible. Although idealised for the purpose of intercomparing models and parameterizations, these cases are based on measurements collected during field experiments. They include nighttime stratocumulus (FIRE), trade wind cumulus (BOMEX), shallow cumulus over land (ARM), and an intermediate regime of cumulus rising into a broken stratocumulus deck (ATEX). The COAMPS-LES results have been evaluated by comparing cloud properties and a number of turbulence statistics with other LES models. The overall agreement is good. Furthermore, only small differences between the two LES subgrid options are observed. The most significant one is the cloud water mixing ratio in the stratiform layer of the ATEX intermediate regime.

Exact numerical budgets of the second and third moments of the vertical velocity have been obtained from COAMPS-LES. They reflect fundamental differences in the turbulence dynamics. Extreme cases are on the one hand the nighttime stratocumulus (FIRE) driven by cloud-top radiative cooling, and on the other hand the trade wind cumulus layer of BOMEX driven by surface fluxes and conditional instability of the atmosphere. The third moment of the vertical velocity ( $\overline{w'^3}$ ) and the skewness ( $Sk_w$ ) are relatively small for the stratocumulus and large for the cumulus layer. The vertical velocity distribution is therefore relatively symmetric for FIRE, but positively skewed for BOMEX with the presence of narrow and strong updraughts balanced by broad and weak downdraughts.

This difference in vertical velocity distribution can be explained by the derived ( $\overline{w'^3}$ ) budget, and in particular by the buoyancy production term in this budget ( $\overline{w'^2\theta'_v}$ ). In BOMEX, it is positive and dominated by the updraught contributions from the surface up to the level of neutral buoyancy. Above that level, the buoyancy term becomes negative due to the contribution of the negatively buoyant downdraughts generated by evaporative cooling. The situation is very different in the stratocumulus case. The magnitude of the buoyancy term is much smaller than in the cumulus case. Both updraughts and downdraughts contribute significantly to the buoyancy throughout the boundary-layer. Their contributions have similar magnitude but opposite signs. The contribution from the downdraughts is always negative and dominates below cloud base. The updraught contribution, which is always positive, dominates in the cloud layer. This leads to a partial cancellation and results in an overall small buoyancy term, which in turn

explains the relatively unskewed vertical velocity distribution in the strato-cumulus compared to the cumulus case.

### Acknowledgements

This work was performed while J.-C. Golaz held a National Research Council Research Associateship Award at the Naval Research Laboratory, Monterey, California. S. Wang acknowledges the support from the Office of Naval Research (ONR) under Program Element (PE) 0602435N. J. D. Doyle was supported by ONR under PE 0601153N. J. M. Schmidt was supported by ONR under PE 062435N. COAMPS<sup>®</sup> is a registered trademark of the Naval Research Laboratory.

### Appendix

We describe how exact numerical budgets for second and third moments are obtained from the LES model. We write the change in vertical velocity  $w$  over a leapfrog time step as:

$$\frac{w_3 - w_1}{2\Delta t} = \sum_k f_{w,k} \quad (\text{A1})$$

where  $w_1$  ( $w_3$ ) represent the vertical velocity at the beginning (end) of the leapfrog time step, and  $f_{w,k}$  the various processes that change  $w$  over the course of the time step [Equation (1),  $i = 3$ ]. We rewrite (A1) as

$$w_3 - w_1 = \sum_k 2\Delta t f_{w,k} \equiv \sum_k \Delta w_k \equiv \Delta w \quad (\text{A2})$$

where we have defined  $\Delta w$  to be the total change consisting of the sum of the process changes  $\Delta w_k$ . We seek to express the change over one time step of the second and third moments of  $w$  as a function of the process changes  $\Delta w_k$ .

The change in the model  $w$  variance over a time step is defined as:

$$\Delta \overline{w'^2} = \overline{w_3'^2} - \overline{w_1'^2} = \overline{(w_3 - \overline{w_3})^2} - \overline{(w_1 - \overline{w_1})^2} = \overline{w_3^2} - \overline{w_3}^2 - \overline{w_1^2} + \overline{w_1}^2. \quad (\text{A3})$$

Here, overbars ( $\overline{w}$ ) denote horizontal averages, and primes ( $w'$ ) are departures from the horizontal averages such that  $w = \overline{w} + w'$ .

Using (A2), we rewrite (A3) in terms of  $w_1$  and  $\Delta w$ :

$$\Delta \overline{w'^2} = 2\overline{w_1 \Delta w} - 2\overline{w_1} \overline{\Delta w} + \overline{\Delta w^2} - \overline{\Delta w}^2. \quad (\text{A4})$$

Similarly we can rewrite (A3) in terms of  $w_3$  and  $\Delta w$ :

$$\Delta \overline{w'^2} = 2\overline{w_3 \Delta w} - 2\overline{w_3} \overline{\Delta w} - \overline{\Delta w^2} + \overline{\Delta w}^2. \quad (\text{A5})$$

Adding (4) and (5) gives:

$$\begin{aligned} \Delta \overline{w'^2} &= \overline{w_1 \Delta w} + \overline{w_3 \Delta w} - \overline{w_1} \overline{\Delta w} - \overline{w_3} \overline{\Delta w} \\ &= \overline{(w_1 + w_3) \Delta w} - (\overline{w_1} + \overline{w_3}) \overline{\Delta w}. \end{aligned} \quad (\text{A6})$$

Replacing  $\Delta w$  by the sum of the separate processes:

$$\begin{aligned} \Delta \overline{w'^2} &= \overline{(w_1 + w_3) \sum_k \Delta w_k} - (\overline{w_1} + \overline{w_3}) \sum_k \overline{\Delta w_k} \\ &= \sum_k \left\{ \overline{(w_1 + w_3) \Delta w_k} - (\overline{w_1} + \overline{w_3}) \overline{\Delta w_k} \right\}. \end{aligned} \quad (\text{A7})$$

This last expression gives the contribution of each individual process  $k$  to the total change of the variance over a time step.

We proceed similarly to obtain the numerical budget for  $\overline{w'^3}$ . The change in the model third moment of  $w$  over a time step is defined as:

$$\begin{aligned} \Delta \overline{w'^3} &= \overline{w_3'^3} - \overline{w_1'^3} \\ &= \overline{(w_3 - w_1)^3} - \overline{(w_1 - w_1)^3} \\ &= \overline{w_3^3} - 3\overline{w_3^2 w_1} + 2\overline{w_3 w_1^2} - \overline{w_1^3} + 3\overline{w_1^2 w_1} - 2\overline{w_1^3}. \end{aligned} \quad (\text{A8})$$

We now use (A2) to rewrite (A8) in terms of  $w_1$  and  $\Delta w$ :

$$\begin{aligned} \Delta \overline{w'^3} &= 3\overline{w_1^2 \Delta w} + 3\overline{w_1 \Delta w^2} + \overline{\Delta w^3} \\ &\quad - 3\overline{w_1^2 \Delta w} - 6\overline{w_1 \Delta w w_1} - 6\overline{w_1 \Delta w} \overline{\Delta w} \\ &\quad - 3\overline{w_1 \Delta w^2} - 3\overline{\Delta w^2 \Delta w} + 6\overline{w_1^2 \Delta w} + 6\overline{w_1 \Delta w^2} + 2\overline{\Delta w^3}. \end{aligned} \quad (\text{A9})$$

Similarly, we rewrite (A8) in terms of  $w_3$  and  $\Delta w$ :

$$\begin{aligned} \Delta \overline{w'^3} &= 3\overline{w_3^2 \Delta w} - 3\overline{w_3 \Delta w^2} + \overline{\Delta w^3} \\ &\quad - 3\overline{w_3^2 \Delta w} - 6\overline{w_3 \Delta w w_3} + 6\overline{w_3 \Delta w} \overline{\Delta w} \\ &\quad + 3\overline{w_3 \Delta w^2} - 3\overline{\Delta w^2 \Delta w} + 6\overline{w_3^2 \Delta w} - 6\overline{w_3 \Delta w^2} + 2\overline{\Delta w^3}. \end{aligned} \quad (\text{A10})$$

Adding (A9) and (A10) and simplifying yields:

$$2\overline{\Delta w'^3} = 3(\overline{w_1^2 + w_3^2})\overline{\Delta w} - 3(\overline{w_1^2} + \overline{w_3^2})\overline{\Delta w} + 6(\overline{w_1^2} + \overline{w_3^2})\overline{\Delta w} - 6\overline{w_1 \Delta w w_1} - 6\overline{w_3 \Delta w w_3} - \overline{(\Delta w - \overline{\Delta w})^3}. \quad (\text{A11})$$

The first five terms on the RHS of (A11) are linear in  $\Delta w$ , therefore the contribution of each process  $k$  to the change in the  $w$  third moment can be readily obtained. Decomposing them gives:

$$\overline{\Delta w'^3} = \sum_k \left\{ \frac{3}{2}(\overline{w_1^2 + w_3^2})\overline{\Delta w_k} - \frac{3}{2}(\overline{w_1^2} + \overline{w_3^2})\overline{\Delta w_k} + 3(\overline{w_1^2} + \overline{w_3^2})\overline{\Delta w_k} - 3\overline{w_1 \Delta w_k w_1} - 3\overline{w_3 \Delta w_k w_3} \right\} - \frac{1}{2}(\overline{\Delta w - \overline{\Delta w}})^3. \quad (\text{A12})$$

The last term on the RHS of (A12) gives the change in the third moment due to the non-linear interaction between processes. We define it as the residual. Note that there is no residual term in the second moment  $w$  budget (A7).

For the purpose of numerical budgets, we define four categories of processes  $\Delta w_k$ . The first four categories arise directly from terms in Equation [(1),  $i = 3$ ]. The advection from the first term on the RHS, the buoyancy from the second term on the RHS, the pressure from the second term on the LHS, and the dissipation from the fourth and fifth terms on the RHS. At the end of the model time step, once  $\Delta w_k$ ,  $w_1$ ,  $w_3$  are all known, we compute the second- and third-moment budgets using (A7) and (A12). The effect of the Robert time filter is computed as the change in  $\overline{w'^2}$ ,  $\overline{w'^3}$  before and after the time filter is applied and is added to the dissipation term.

## References

- André J. C., de Moor, G., Lacarrère P., and du Vachat, R. 1976, 'Turbulence Approximation for Inhomogeneous Flows: Part I. The Clipping Approximation', *J. Atmos. Sci.* **33**, 476–481.
- Beare R. J., Mac Vean, M. K., Holtslag, A. A. M., Cuxart, J., Esau, I., Golaz, J.-C., Jimenez, M. A., Khairoutdinov, M., Kosovic, B., Lewellen, D., Lund, T. S., Lundquist, J. K., McCabe, A., Moene, A. F., Noh, Y., Raasch, S., and Sullivan, P.: 2005, 'An Intercomparison of Large-Eddy Simulations of the Stable Boundary-Layer', *Boundary-Layer Meteorology*, in press.
- Bott, A.: 1989a, 'A Positive Definite Advection Scheme Obtained by Nonlinear Renormalization of the Advective Fluxes', *Mon. Wea. Rev.* **117**, 1006–1015.
- Bott, A.: 1989b, 'Reply', *Mon. Wea. Rev.* **117**, 2633–2636.
- Brown, A. R., Cederwall, R. T., Chlond, A., Duynkerke, P. G., Golaz, J.-C., Khairoutdinov, M., Lewellen, D. C., Lock, A. P., MacVean, M. K., Moeng, C.-H., Neggers, R. A. J., Siebesma, A. P., and Stevens, B., 2002, 'Large-Eddy Simulation of the Diurnal Cycle of Shallow Cumulus Convection Over Land', *Quart. J. Roy. Meteorol. Soc.* **128**, 1075–1093.
- Brown, A. R., Derbyshire, S. H., and Mason, P. J. 1994, 'Large-Eddy Simulation of Stable Atmospheric Boundary Layers with a Revised Stochastic Subgrid Model', *Quart. J. Roy. Meteorol. Soc.* **120**, 1485–1512.

- Cuijpers, J. W. M. and Duynkerke, P. G.: 1993, 'Large Eddy Simulation of Trade Wind Cumulus Clouds', *J. Atmos. Sci.* **50**, 3894–3908.
- Cuijpers, J. W. M., Duynkerke, P. G., and Nieuwstadt, F. T. M.: 1996, 'Analyses of Variance and Flux Budgets in Cumulus-Topped Boundary Layers', *Atmos. Res.* **40**, 307–337.
- de Roode, S. R. and Bretherton, C. S.: 2003, 'Mass-Flux Budgets of Shallow Cumulus Clouds', *J. Atmos. Sci.* **60**, 137–151.
- Deardorff, J. W.: 1980, 'Stratocumulus-Capped Mixed Layers Derived From a Three-Dimensional Model', *Boundary-Layer Meteorol.* **18**, 495–527.
- Glendening, J. W. and Haack, T.: 2001, 'Influence of Advection Differencing Error Upon Large-Eddy Simulation Accuracy', *Boundary-Layer Meteorol.* **98**, 127–153.
- Golaz, J.-C., Larson, V. E., and Cotton, W. R.: 2002, 'A PDF Based Model for Boundary-Layer Clouds. Part I: Method and Model Description', *J. Atmos. Sci.* **59**, 3540–3551.
- Grant, A. L. M. and Brown, A. R.: 1999, 'A Similarity Hypothesis for Shallow-Cumulus Transports', *Quart. J. Roy. Meteorol. Soc.* **125**, 1913–1936.
- Grant, A. L. M. and Lock, A. P.: 2004, 'The Turbulent Kinetic Energy Budget for Shallow Cumulus Convection', *Quart. J. Roy. Meteorol. Soc.* **130**, 401–422.
- Hodur, R. M.: 1997, 'The Naval Research Laboratory's Coupled Ocean/Atmosphere Mesoscale Prediction System (COAMPS)', *Mon. Wea. Rev.* **125**, 1414–1430.
- Klemp, J. B. and Wilhelmson, R. B.: 1978, 'The Simulation of Three-Dimensional Convective Storm Dynamics', *J. Atmos. Sci.* **35**, 1070–1095.
- Lappen, C.-L. and Randall, D. A.: 2001, 'Toward a Unified Parameterization of the Boundary-Layer and Moist Convection. Part I: A New Type of Mass-Flux Model', *J. Atmos. Sci.* **58**, 2021–2036.
- Lilly, D. K.: 1962, 'On the Numerical Simulation of Buoyant Convection', *Tellus* **14**, 148–172.
- Mason, P. J.: 1994, 'Large-Eddy Simulation: A Critical Review of the Technique', *Quart. J. Roy. Meteorol. Soc.* **120**, 1–26.
- Moeng, C.-H.: 1986, 'Large-Eddy Simulation of a Stratus-Topped Boundary Layer. Part I: Structure and Budgets', *J. Atmos. Sci.* **43**, 2886–2900.
- Moeng, C.-H., Cotton, W. R., Bretherton, C., Chlond, A., Kairoutdinov, M., Krueger, S., Lewellen, W. S., MacVean, M. K., Pasquier, J. R. M., Rand H. A., Siebesma, A. P., Stevens, B., and Sykes, R. I.: 1996, 'Simulation of a Stratocumulus-Topped Planetary Boundary Layer: Intercomparison Among Different Numerical Codes', *Bull. Amer. Meteorol. Soc.* **77**, 261–278.
- Nicholls, S., Lemone, M. A., and Sommeria, G.: 1982, 'The Simulation of a Fair Weather Marine Boundary-Layer in GATE Using a Three-Dimensional Model', *Quart. J. Roy. Meteorol. Soc.* **108**, 167–190.
- Siebesma, A. P., Bretherton, C. S., Brown, A., Chlond, A., Cuxart, J., Duynkerke, P. G., Jiang, H., Khairoutdinov, M., Lewellen, D., Moeng, C.-H., Sanchez, E., Stevens, B., and Stevens, D. E.: 2003, 'A Large Eddy Simulation Intercomparison Study of Shallow Cumulus Convection', *J. Atmos. Sci.* **60**, 1201–1219.
- Smagorinsky, S.: 1963, 'General Circulation Experiments With the Primitive Equations', *Mon. Wea. J. Rev.* **91**, 99–164.
- Sommeria, G.: 1976, 'Three-Dimensional Simulation of Turbulent Processes in an Undisturbed Trade Wind Boundary Layer', *J. Atmos. Sci.* **33**, 216–241.
- Stevens, B., Ackerman, A. S., Albrecht, B. A., Brown, A. R., Chlond, A., Cuxart, J., Duynkerke, P. G., Lewellen, D. C., MacVean, M. K., Neggers, R. A. J., Sánchez, E., Siebesma, A. P., and Stevens, D. E.: 2001, 'Simulations of Trade Wind Cumuli Under a Strong Inversion', *J. Atmos. Sci.* **58**, 1870–1891.

- Stevens, B., Lenschow, D. H., Vali, G., Gerber, H., Bandy, A., Blomquist, B., Brenguier, J.-L., Bretherton, C. S., Burnet, F., Campos, T., Chai, S., Faloona, I., Friesen, D., Haimov, S., Laursen, K., Lilly, D., Loehrer, S. M., Malinowski, S. P., Morley, B., Petters, M. D., Rogers, H., Russell, L., Savic-Jovicic, V., Snider, J. R., Straub, D., Szumowski, M. J., Takagi, H., Thornton, D. C., Tschudi, M., Twohy, C., Wetzel, M., van Zanten, M. C., 'Dynamics, and Chemistry of Marine Stratocumulus – DYCOMS-II', *Bull. Amer. Meteorol. Soc.* **84**, 579–593.
- Stevens B., Moeng, C.-H., Ackerman, A. S., Bretherton, C. S., Chlond, A., de Roode, S., Edward, J., Golaz, J.- C., Diang, H., Khairontdinor, M., Kirkpatrick, M. P., Lewellen, D. C., Lock, A., Müller, F., Stevens, D. E., Whelan, E., and Zhu, P., 2005, 'Evaluation of Large-Eddy Simulation via Observations of nocturnal Marine Stratocumulus', *Misc. Wea. Rev.*, **133**, 1443–1462.
- Stevens B., Moeng, C.-H., and Sullivan, P. P., 1999, 'Large-Eddy Simulations of Radiatively Driven Convection: Sensitivities to the Representation of Small Scales', *J. Atmos. Sci.* **56**, 3963–3984.
- Stull, R. B.: 1988, *An Introduction to boundary-layer Meteorology*. Kluwer Academic Publishers, Dordrecht, 666 pp.
- Wang, S. and Stevens, B.: 2000, 'Top-Hat Representation of Turbulence Statistics in Cloud-Topped Boundary-Layers: A Large Eddy Simulation Study'. *J. Atmos. Sci.* **57**, 423–441.